Exospheric Temperature Measured by NASA-GOLD Under Low Solar Activity Comparison With Other Data Sets

Park, Jaeheung; Evans, Joseph S.; Eastes, Richard W.; Lumpe, Jerry D.; van den Ijssel, Jose; Englert, Christoph R.; Stevens, Michael H.

Important note
To cite this publication, please use the final published version (if applicable).
Please check the document version above.

Correspondence to:

J. Park,
pj@kasi.re.kr

Exospheric Temperature Measured by NASA-GOLD Under Low Solar Activity: Comparison With Other Data Sets

Jaeheung Park[1,2], **Joseph S. Evans[3]**, **Richard W. Eastes[4]**, **Jerry D. Lumpe[5]**, **Jose van den Ijssel[6]**, **Christoph R. Englert[7]**, and **Michael H. Stevens[7]**

[1]Space Science Division, Korea Astronomy and Space Science Institute, Daejeon, South Korea, [2]Department of Astronomy and Space Science, Korea University of Science and Technology, Daejeon, South Korea, [3]Computational Physics Inc., Springfield, VA, USA, [4]Laboratory for Atmospheric and Space Physics, University of Colorado Boulder, Boulder, CO, USA, [5]Computational Physics Inc., Boulder, CO, USA, [6]Faculty of Aerospace Engineering, Delft University of Technology, Delft, The Netherlands, [7]Space Science Division, U.S. Naval Research Laboratory, Washington, DC, USA

Abstract Exospheric temperature is one of the key parameters in constructing thermospheric models and has been extensively studied with in situ observations and remote sensing. The Global-scale Observations of the Limb and Disk (GOLD) at a geosynchronous vantage point provides dayglow limb images for two longitude sectors, from which we can estimate the terrestrial exospheric temperature since 2018. In this paper, we investigate climatological behavior of the exospheric temperature measured by GOLD. The temperature has positive correlations with solar and geomagnetic activity and exhibits a morning-afternoon asymmetry, both of which agree with previous studies. We have found that the arithmetic sum of $F_{10.7}$ (solar) and Ap (geomagnetic) indices is highly correlated with the exospheric temperature, explaining ~64% of the day-to-day variability. Furthermore, the exospheric temperature has good correlation with thermospheric parameters (e.g., neutral temperature, O_2 density, and NO emission index) sampled at various heights above ~130 km, in spite of the well-known thermal gradient below ~200 km. However, thermospheric temperature at altitudes around 100 km is not well correlated with the GOLD exospheric temperature. The result implies that effects other than thermospheric heating by solar Extreme Ultraviolet and geomagnetic activity take control below a threshold altitude that exists between ~100 and ~130 km.

Plain Language Summary In the terrestrial thermosphere, which is the topmost layer of the collisional atmosphere surrounding the Earth, temperature generally increases with altitude unlike in the troposphere near the surface. However, the thermospheric temperature does not increase indefinitely, but approaches an asymptote, which is referred to as the exospheric temperature, the temperature of the outermost layer of the atmosphere. The Global-scale Observations of the Limb and Disk (GOLD) instrument, launched into a geosynchronous orbit in 2018, regularly observes atmospheric glow from the Earth's limb, from which we can estimate the terrestrial exospheric temperature (T_{exo}). The GOLD T_{exo} is higher in the afternoon than in the morning and generally increases as solar radiation strength or geomagnetic field variability increases. In this paper, we show that a simple arithmetic sum of the solar and geomagnetic indices can explain a large part of the day-to-day T_{exo} variability. Also, T_{exo} has good (poor) correlation with thermospheric parameters such as temperature and density above ~130 km (at ~100 km). The behavior suggests that factors other than solar radiation and geomagnetic energy deposition, both of which are correlated well with T_{exo}, take control below a threshold altitude that is between ~100 and ~130 km.

1. Introduction

1.1. Exospheric Temperature (T_{exo})

Exospheric temperature (T_{exo}) is the asymptotic limit that the thermospheric temperature approaches with increasing height (Swenson, 1969, Equation 1). It is an important parameter when characterizing the whole thermosphere. To describe thermospheric status, most empirical models, including the well-known Mass-Spectrometer-Incoherent-Scatter (MSIS) model (e.g., Emmert et al., 2021), start by specifying exospheric temperature, from which altitude-dependent temperature and density are subsequently determined (e.g., Stock, 2017, Section 4.3; https://www.spenvis.oma.be/help/background/atmosphere/models.html). Exospheric temperatures have also been investigated for other planets, such as Venus and Mars (Bougher et al., 2009, Figure 1; Forbes et al., 2008,

Figure 3; Lichtenegger et al., 2006, Figure 4), which also exhibit significant dependence on solar radiation; see also Bougher et al. (2017, Figure 8).

1.2. Previous Observational Studies on Exospheric Temperature

Until now, estimating terrestrial T_{exo} from observation data can be largely categorized into the three families: (a) methods based on plasma diagnoses by ground-based radar facilities or ionosondes (e.g., Kelley et al., 1983; Mikhailov & Perrone, 2016), (b) usage of thermospheric mass density or orbit drag data combined with empirical thermospheric models (e.g., Weng et al., 2017), and (c) limb airglow imaging (Evans et al., 2020).

First, estimating T_{exo} from Incoherent Scatter Radar (ISR) data starts from fitting models of ion thermodynamics and chemistry to measured ion temperature profiles (e.g., Picone et al., 2002, Section 4.3). Kelley et al. (1983) and Buonsanto and Pohlman (1998) extracted T_{exo} from ISR observations at Chatanika and Millstone Hill, respectively. On the other hand, Mikhailov and Perrone (2016) deduced T_{exo} by fitting thermospheric parameters to time series of ionosonde data.

Second, there are T_{exo} estimation methods based on in situ observations of thermospheric mass density, which can be combined with thermospheric models such as MSIS. The method was applied to thermospheric mass density provided by onboard accelerometers or by orbit element information (Forbes et al., 2011; Weimer et al., 2016, 2020; Weng et al., 2017). As the spacecraft data can cover the whole globe including oceanic areas, extensive climatological studies were conducted using those data sets.

Among the three methods, the last one (limb imaging) has not been thoroughly exploited. To the best of the authors' knowledge, only a few papers have addressed the problem of deriving T_{exo} from limb imaging. Meier et al. (2005, 2015) estimated T_{exo} from the limb airglow profiles obtained by the Global ultraviolet imager (GUVI) onboard Thermosphere, Ionosphere, Mesosphere Energetics & Dynamics (TIMED) satellite. Evans et al. (2020) applied similar remote sensing retrieval methods to limb observations by the Global-scale Observations of the Limb and Disk (GOLD). Both Meier et al. (2005, 2015) and Evans et al. (2020) demonstrated that T_{exo} is positively correlated with geomagnetic activity (Ap index) and solar radiation ($F_{10.7}$ index).

1.3. Room for Further Improvement

As mentioned above, there already are many studies which observationally determined T_{exo} and constructed its climatological behavior. Still, there is room for further improvement on this topic. For example, ground-based studies using ISR or ionosonde data (e.g., Kelley et al., 1983) do not provide global coverage. Specifically, there are large data gaps above the oceans. Similarly, in studies based on in situ observations of thermospheric mass density (e.g., Weimer et al., 2020), the actual data were limited to only one or two altitudes. That is to say, reconstructed height profiles of the thermosphere inevitably depended on the models adopted in those studies. Also, when two satellites are used, intercalibration between the data sets should be considered carefully (e.g., Weimer et al., 2016). As for limb observations of airglow, the data provide densely sampled vertical profiles of the thermosphere, which would be beneficial in determining T_{exo} accurately. While large databases of limb scan data do exist, the existing literature on limb-based T_{exo} estimation has room for improvement. For example, Meier et al. (2005) only addressed a case during a geomagnetic storm. Meier et al. (2015) conducted statistical analyses of T_{exo}, but their Figure 20 only showed yearly averaged values (i.e., one value per year). Evans et al. (2020) was the first statistical study on T_{exo} provided by GOLD. They investigated the dependence of T_{exo} on local time (LT), latitude/longitude, and geomagnetic/solar activity. Still, only 1.5 years of the GOLD observations (October 2018 to February 2020) were used in that study, which were mostly restricted to very low solar activity near solar minimum.

Hence, in this paper, we show statistical investigations of the GOLD T_{exo} data, which extend the results of Evans et al. (2020) in the following two ways. First, we use GOLD observations over an extended period of time: from October 2018 to July 2021. This enables us to include T_{exo} for higher solar activity conditions than analyzed by Evans et al. (2020) in the statistics. The maximum $F_{10.7}$ index for the period addressed in Evans et al. (2020) is 81.8 (16 October 2018 to 02 February 2020) while that of our study is 113.1. Second, we cross-compare the T_{exo} data with other data sets: e.g., thermospheric mass density observed by Swarm satellites and O_2 density retrieved from GOLD stellar occultation measurements.

In Section 2, we briefly describe the instruments and data sets used in this study. Section 3 presents the general climatology of the GOLD T_{exo} data and its dependence on, e.g., latitude, longitude, local time, season, and solar/geomagnetic activity. Also, GOLD T_{exo} data are compared with other thermospheric observations, and their correlations are addressed. In Section 4, we discuss the results shown in Section 3, from which conclusions will be drawn in Section 5.

2. Instruments and Data Sets Used

GOLD, which images the Earth's disk and limb in the Far-Ultraviolet (FUV), was launched onboard the SES-14 satellite to a geosynchronous orbit at 47.5°W longitude in January 2018. The spectral wavelength range of GOLD is from 134.5 to 162 nm, which covers the commonly used oxygen 135.6 nm line and the molecular nitrogen (N_2) Lyman-Birge-Hopfield (LBH) band system. From the limb scan images for 100–300 km tangent altitudes, one can retrieve exospheric temperature (T_{exo}) on the dayside (Evans et al., 2020). In addition, GOLD provides disk images of daytime thermospheric neutral temperature at heights of ~150 km (T_{disk}): see Eastes et al. (2020, Figure 3). From stellar occultation data, one can also retrieve the O_2 density between about 130-km and 200-km altitude on both the dayside and nightside limbs (Lumpe et al., 2020).

In this study, we use the three GOLD Level-2 data sets: (a) exospheric temperature (product name: TLIMB), (b) daytime thermospheric neutral temperature at ~150 km (product name: TDISK), and (c) O_2 density (product name: O2DEN). All GOLD data are publicly available at: https://gold.cs.ucf.edu/data/search/. Note that the limb scan, disk scan, and stellar occultation data of GOLD are restricted to a range of geographic longitude (GLON) due to its geosynchronous vantage point: e.g., Eastes et al. (2020, Figure 5). For details, readers can consult the product guides that are available at the official repository: https://gold.cs.ucf.edu/data/documentation/.

The Swarm mission is composed of three identical satellites (Alpha, Bravo, and Charlie) that were launched into polar, circular Low-Earth-Orbits (LEOs) on 22 November 2013. Among other instruments, the onboard accelerometer can provide in situ thermospheric mass density every 10 s (product name: DNSxACC where x is either A, B, or C representing one specific satellite). As the accelerometer data quality is best for Swarm-Charlie among the three spacecraft (Siemes et al., 2016), only the DNSCACC product (i.e., mass density data from Swarm-Charlie) is available to the public at present, which is used in this study. Since April 2014, when the commissioning phase was completed, Swarm-Charlie was stationed at altitudes around 450 km. The local time (LT) of Swarm-Charlie precesses slowly. All the LT sectors can be covered within ~130 days, when the northward and southward passes are combined together. All the data used in this study are available at: https://swarm-diss.eo.esa.int/#swarm%-2FLevel2daily%2FLatest_baselines%2FDNS%2FACC, which provided the thermospheric density data from 01 February 2014 to 31 May 2021.

The science target of the Ionospheric Connection Explorer (ICON) mission is low-latitude/midlatitude ionospheric/thermospheric coupling processes. The satellite is in a circular orbit at an altitude of about 590 km with an orbit inclination of 27°, allowing for limb observations between 13°S and 43°N. The ICON half-precession period for sampling all locations and local times is about 27 days (Immel et al., 2018), depending on latitude. Among a suite of science instruments, the Michelson Interferometer for Global High-resolution Thermospheric Imaging (MIGHTI) observes green (557.7 nm), red (630 nm), and near-infrared (IR; O_2 A-band around 762 nm) airglow, from which neutral wind vectors and neutral temperatures can be derived as a function of height (Englert et al., 2017). Wind and temperature data are measured parallel to the spacecraft trajectory, on the limb. ICON has two MIGHTI sensor units, MIGHTI-A and MIGHTI-B, which produce temperature data independently of each other. Here, we use the Level 2 neutral temperature data of ICON/MIGHTI-A (Version 05), which can be downloaded from ftp://icon-science.ssl.berkeley.edu/pub/LEVEL.2/MIGHTI/. Though the temperature data can cover altitude ranges between about 90 and 140 km, currently available temperature products only cover the altitude range between 90–127 km during daytime and 90–108 km during nighttime, which is slightly lower than that of GOLD O2DEN data (130–200 km). We conservatively set the altitude range used in this study to 100 ± 10 km. While the nominal precision is typically <1 K at 100 km, the systematic uncertainty for the Version 05 product is about 3 K at 100 km and depends on local time. For details, readers are referred to Stevens et al. (2018) and the product description available at ftp://icon-science.ssl.berkeley.edu/pub/Documentation/ICON_L2-3_MIGHTI-A_Temperature_v05.pdf.

The Aura satellite is in a Sun-synchronous orbit at an altitude of about 710 km (local time: 13:45 and 01:45). Since launch in July 2004, the onboard Microwave Limb Sounder (MLS) has continuously monitored the Earth's limb in the microwave range, from which we can derive neutral temperature up to about 100 km (Schwartz et al., 2008; Shepherd et al., 2020). According to Schwartz et al. (2008), the precision of the Aura/MLS temperature is about 1–3 K. Aura/MLS Level-3 data provide daily zonal-mean temperature as a function of geographic latitude at multiple altitude levels. In this study, the Level-3 temperature data between 2018 and 2020 are used, which are available after registration at https://acdisc.gesdisc.eosdis.nasa.gov/data/Aura_MLS_Level3/ML3DZT.005/.

The TIMED satellite, which was launched in December 2001, has been monitoring the terrestrial ionosphere/thermosphere from an altitude of 625 km for about 2 decades. Its LT is not fixed due to the orbit inclination of 74.1°, and TIMED covers all LT sectors in about 60 days. The onboard Sounding of the Atmosphere using Broadband Emission Radiometry (SABER) instrument measures limb images in the IR range (1.27–17 μm): http://saber.gats-inc.com/. The instrument provides the Thermosphere Climate Index (TCI), which represents daily values of global IR cooling power in units of Watt (Mlynczak et al., 2018a). We use the SABER TCI data downloaded from https://www.spaceweather.com/images2021/08sep21/tci_info.txt.

Throughout this paper, we use three seasons: June and December solstices and the combined equinox. June (December) solstice is defined as the months from May to August (from November to February of the next year). The combined equinox consists of the remaining months (March-April and September-October). This three-season convention is commonly used in the space science community: e.g., in Li et al. (2018), Lühr et al. (2019), and Kil et al. (2020), to name a few.

3. Results

In this section, we present statistical analysis results of GOLD T_{exo} (Sections 3.1–3.2) as well as other satellite data (Section 3.3). Note that most of the statistical analyses contained herein assume a Gaussian distribution of parent population sampling. For correlation coefficient, we use the "corrcoef" function of MATLAB that gives the Pearson correlation coefficients.

3.1. General Climatology of GOLD T_{exo}

Figure 1 presents GOLD T_{exo} as a function of solar local time (SLT; horizontal axis) and geographic latitude (GLAT; vertical axis). Data from the western and eastern limbs are presented in Figures 1a–1c and 1d–1f, respectively. Note that the GOLD T_{exo} data are limited to near-equatorial regions (e.g., Eastes et al., 2020, Figure 5) and dayside (Evans et al., 2020). Each panel in Figures 1a–1c (and Figures 1d–1f) represents a season: (a and d) combined equinoxes, (b and e) June solstice, and (c and f) December solstice. In Figure 1, four features are of note. First, the afternoon T_{exo} is higher than before noon by several tens of Kelvins. Using the bin average values shown in Figures 1a–1c, we estimate the mean and standard deviations of the prenoon and postnoon T_{exo}. The results are 796 ± 39, 790 ± 40, 804 ± 40 K and 817 ± 34, 813 ± 40, 829 ± 35 K, respectively. Similarly in Figures 1d–1f, the prenoon and postnoon T_{exo} is 787 ± 37, 793 ± 43, 794 ± 33 K and 861 ± 49, 857 ± 43, 866 ± 55 K, respectively. Second, equatorial (|GLAT| < 5°) T_{exo} is higher than corresponding off-equatorial (|GLAT| ≥ 5°) values. Using the bin average values shown in Figures 1a–1c, we derive the mean and standard deviations of the equatorial and off-equatorial T_{exo}. The results are 846 ± 19, 841 ± 19, 854 ± 20 K and 785 ± 29, 777 ± 31, 794 ± 31 K, respectively. Similarly in Figures 1d–1f, the equatorial and off-equatorial T_{exo} is 854 ± 51, 849 ± 42, 861 ± 49 K and 830 ± 58, 831 ± 55, 834 ± 62 K, respectively. Third, seasonal variations are inconspicuous, possibly reflecting the low latitudes of the data. In Figures 1a–1c, the mean and standard deviation of all the pixels in each panel are 804 ± 53, 797 ± 56, 812 ± 56 K. In Figures 1d–1f, the values are 835 ± 67, 835 ± 63, 840 ± 69 K. The differences between seasons (e.g., between Figures 1a and 1b) generally stay within ±10 K. Fourth, T_{exo} from the western limb (Figures 1a–1c) is not exactly the same as from the eastern limb (Figures 1d–1f), which will be described in detail in Figures 2 and 3.

In Figures 2a and 2b, the GOLD T_{exo} is presented again, but as a function of SLT (vertical axis) and date (horizontal axis). Panels a and b, respectively, correspond to the western (Pacific) and eastern (African) limb data (Eastes et al., 2020, Figure 5). Daily averaged T_{exo} is presented in panel c as a black curve while Ap indices are shown in magenta. The bottom panel displays $F_{10.7}$ indices. In Figure 2c, the most conspicuous feature is the good correlation between T_{exo} and Ap index until mid-2020 (i.e., around the solar minimum): the correlation
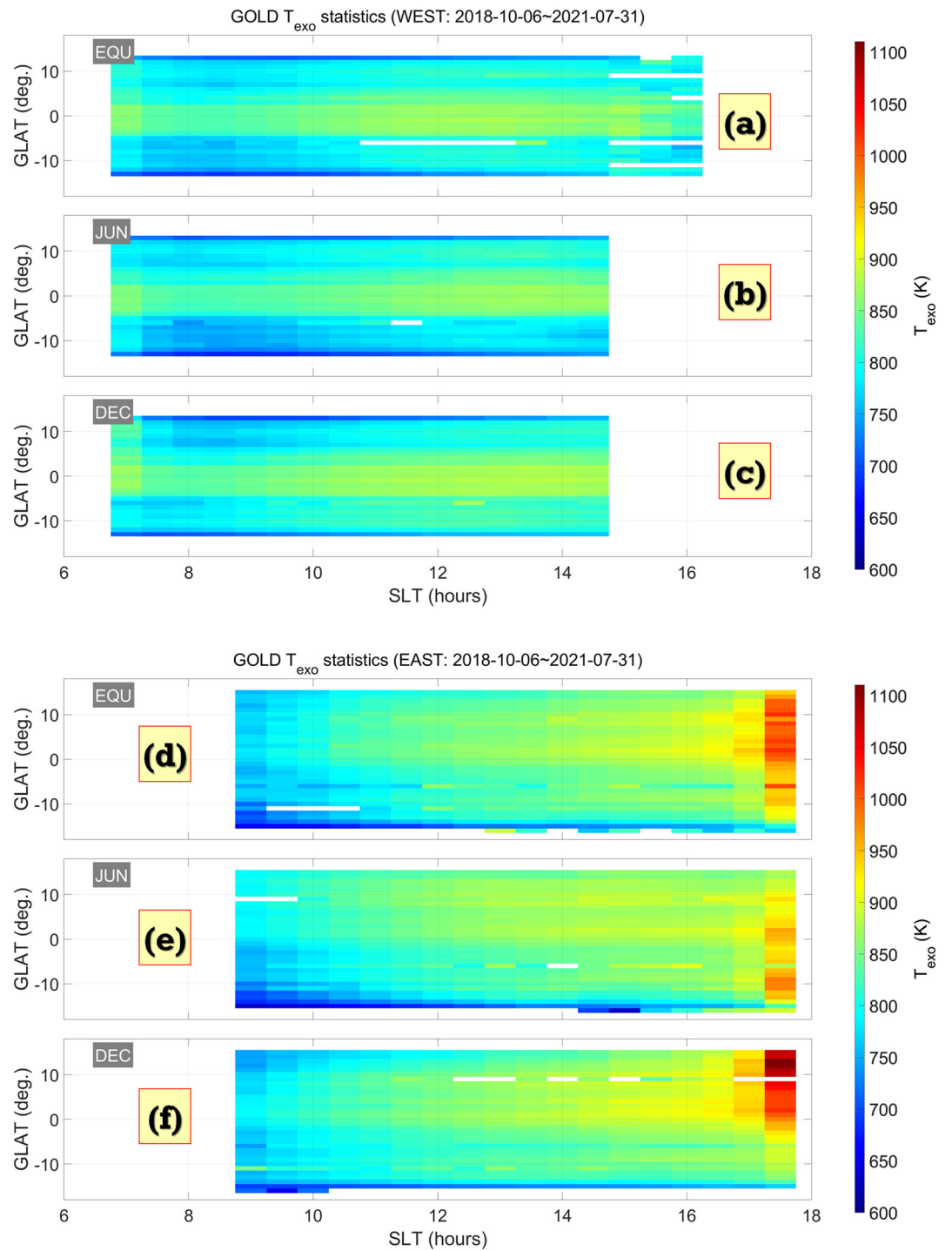
Figure 1. Average T_{exo} as a function of solar local time (x axis) and geographic latitudes (y axis). GOLD limb observations between 100 and 300 km tangent altitudes are used for T_{exo} derivation (Evans et al., 2020). Panels a–c represent combined equinoxes, June solstice, and December solstice, respectively, for the GOLD western limb. Panels d–f have the same structure, but for the GOLD eastern limb. Note that only daytime data exist for T_{exo}.

coefficient between the two is 0.59. After September 2020, the correlation becomes slightly compromised as the overall $F_{10.7}$ index increases with significant fluctuations (Figure 2d). After 01 September 2020, the correlation coefficient between T_{exo} and Ap is only 0.37. Rather, the T_{exo} seems to be correlated with both Ap and $F_{10.7}$: see,

Figure 2. The top two panels present average T_{exo} as a function of solar local time (SLT; y axis) and date (x axis), averaged over all latitudes. Panels a–b present T_{exo} from the western and eastern limb of GOLD, respectively. White areas correspond to data gaps. Note that the western (eastern) limb data in panel a (panel b) cover earlier (later) LTs close to the sunri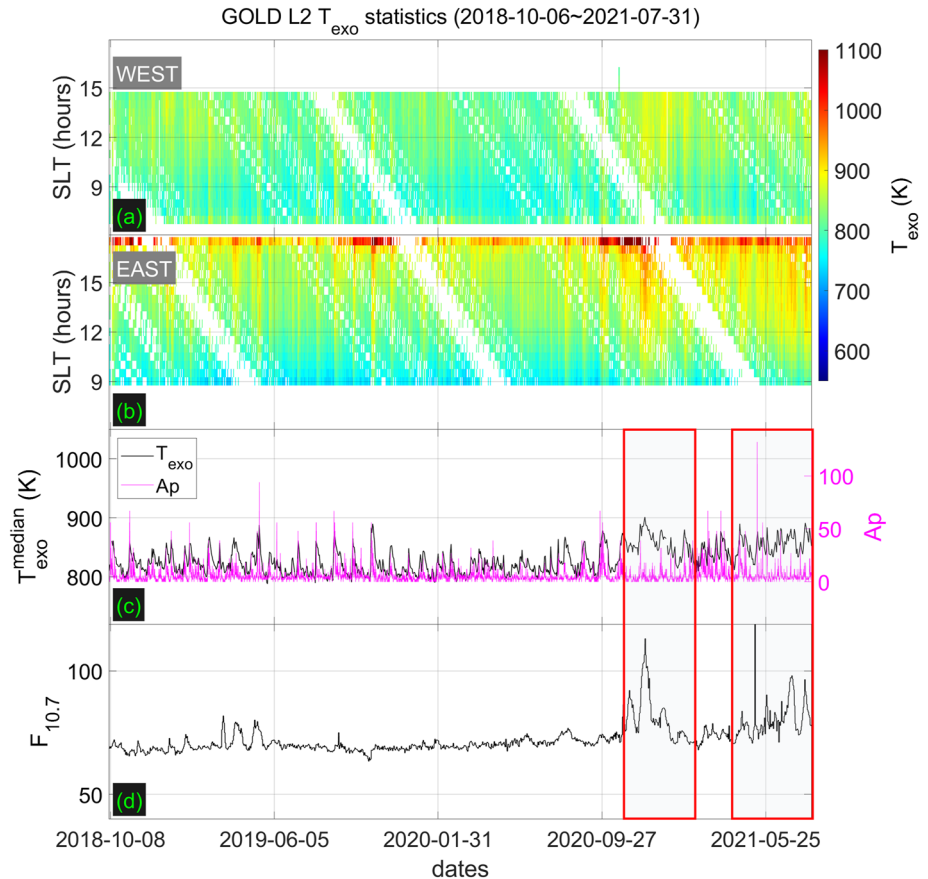se (sunset), which results from the operation scenario of GOLD. Panel c shows daily averages of T_{exo} over all LTs and latitudes (black curve corresponds to the left axis) as well as Ap indices (magenta curve to the right axis). In panel d, we show $F_{10.7}$ indices. The red rectangles mark periods of enhanced $F_{10.7}$ index.

e.g., the red rectangles on the right-hand side (Figures 2c and 2d). This behavior will be addressed quantitatively in Figures 4 and 5.

Another notable feature in Figures 2a and 2b is the fact that T_{exo} at a fixed date and SLT differs between the eastern limb (Figure 2b; ~30°E GLON) and the western limb (Figure 2a; ~130°W GLON). Figure 3 presents histograms of the T_{exo} difference between the eastern and western limb exhibited in Figure 2 (i.e., $T_{exo}^{east} - T_{exo}^{west}$): (a) 9.5 SLT, (b) 14.5 SLT, and (c) all relevant SLTs. Before noon (Figure 3a), T_{exo} is lower on the eastern limb than on the west: e.g., by about −25 K at 9.5 SLT. Past noon, this trend is reversed: e.g., by about +31 K at 14.5 SLT. This east-west difference was also evident in Figure 1 if we compare Figures 1a–1c with Figures 1d–1f. Between 09 and 15 SLT, T_{exo} is derived from both limb data sets while before 09 SLT (after 15 SLT) only the western (eastern) limb is used.

First, one may attribute the difference between the eastern and western limb observations to nonmigrating tidal signatures (i.e., longitude dependence at a fixed SLT) in the upper thermosphere, as shown in Liu et al. (2009). However, total neutral mass density in the postnoon equatorial upper thermosphere (Liu et al., 2009, Figure 1b), which is expected to correlated with postnoon T_{exo}, is not much higher at the GOLD eastern limb location (30°E GLON) than at the western (~130°W GLON) limb: the nonmigrating tidal signatures cannot clearly explain the east-west difference of GOLD T_{exo}. Second, the east-west difference may be connected to dependence of thermospheric mass density on *magnetic* latitudes (Liu et al., 2009, Figure 1b). Note that the geographic equator at the GOLD eastern limb (30°E GLON) is farther from the *magnetic* equator than at the western limb. However,
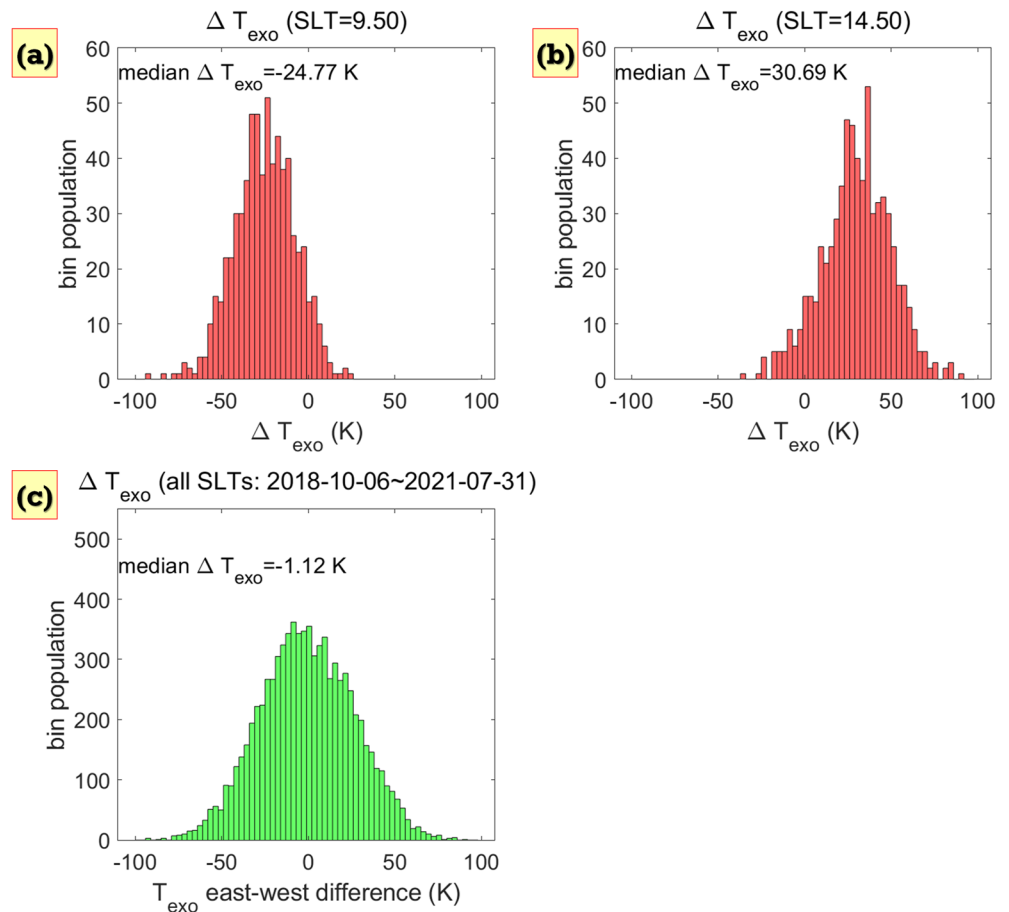
Figure 3. Histograms of T_{exo} difference between the GOLD eastern and western limb data in Figures 2a and 2b: (a) 9.5 SLT, (b) 14.5 SLT, and (c) all relevant SLTs. Negative values signify western-limb T_{exo} being larger than the eastern one.

the effect of *magnetic* latitudes as in Liu et al. (2009, Figure 1b), if any, would mean T_{exo} after 15 SLT (with only eastern-limb data) would increase from the geographic equator to the south (i.e., moving farther from the *magnetic* equator). As this expectation is not confirmed by Figure 1, the east-west difference in Figure 2 cannot be interpreted as geophysical effects of *magnetic* latitudes.

Currently, we do not have a conclusive interpretation for this peculiarity. The east-west difference may imply either the need for improvement of the T_{exo} retrieval algorithm or some unresolved instrument calibration issues in the underlying Level 1C limb radiance data. In Figure 3c, the median value of the east-west difference is only about −1.1 K when we consider both prenoon and postnoon data points. In the following analyses, we average the data from both limbs.

In a similar context, T_{exo} around 18 SLT in Figures 1d–1f (eastern limb; Figure 2b) staying around 1,000 K appears unexpectedly high, as will be demonstrated later by the MSIS predictions in Section 4.3. This duskside hotspot also appears in Evans et al. (2020, Figure 7). Note that the 18 SLT in the eastern limb is at the edge of the GOLD scan area and the border of daytime (GOLD T_{exo} algorithm is designed only for daytime conditions). The exact source of this hotspot is currently under investigation. It is encouraging that the hotspot intensity varies with T_{exo} at earlier SLTs in Figure 2 (i.e., the hotspots seem to reflect T_{exo} at least qualitatively), but reliability of their *absolute* magnitude requires further investigation.
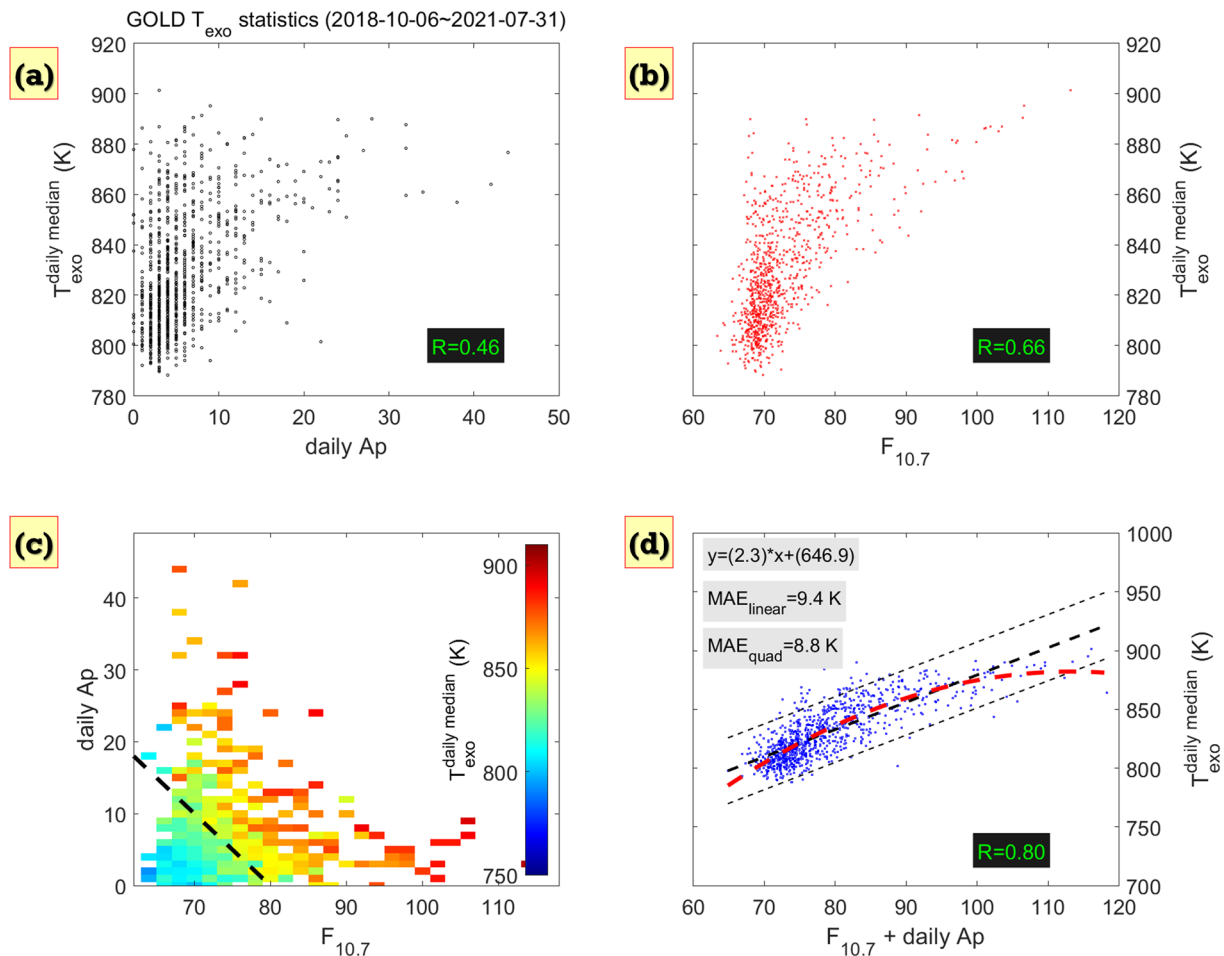
Figure 4. Correlation diagrams of T_{exo} with selected geophysical indices: (a) scatterplot of T_{exo} versus daily Ap, (b) scatterplot of T_{exo} versus $F_{10.7}$, (c) T_{exo} distribution as a function of daily Ap and $F_{10.7}$, and (d) scatterplot of T_{exo} versus (daily Ap + $F_{10.7}$). The black dashed line in panel (c) is given to guide readers' eyes on the general trend of the T_{exo} distribution in the Ap − $F_{10.7}$ space. The thick black dashed line in panel d corresponds to the linear regression, whose equation and Mean-Absolute-Error (MAE$_{linear}$) are annotated inside the panel. The thin black dashed lines mark the 95% prediction interval. The red dashed line in panel d represents the quadratic fit, of which the Mean-Absolute-Error (MAE$_{quad}$) is also shown.

3.2. Dependence of GOLD T_{exo} on Solar/Geomagnetic Activities

Figures 4a and 4b are scatterplots of daily averaged GOLD T_{exo} and daily indices of Ap (panel a) and $F_{10.7}$ (panel b), both of which are obtained from https://omniweb.gsfc.nasa.gov/. According to the description at https://omniweb.gsfc.nasa.gov/html/ow_data.html, the $F_{10.7}$ is adjusted to 1 Astronomical Unit (AU). All seasons are combined together in Figure 4 because of the weak seasonal variations of GOLD T_{exo} as demonstrated in Section 3.1. In each panel, a correlation coefficient is given between the horizontal-axis and vertical-axis data. We can see that T_{exo} exhibits positive correlations with both daily Ap (panel a: the correlation coefficient $R = 0.46$) and $F_{10.7}$ (panel b: $R = 0.66$) indices. In Figure 4c, the GOLD T_{exo} (color palette) is shown as a function of both $F_{10.7}$ (horizontal axis) and Ap (vertical axis). The black dashed line represents a condition that Ap + $F_{10.7}$ is a constant. In Figure 4c, we find that the T_{exo} distribution is largely aligned with the black dashed guide line and its parallels: i.e., the black dashed line can be approximately considered as one of the iso-T_{exo} lines. This feature means that T_{exo} can be expressed as a simple arithmetic sum of Ap and $F_{10.7}$. Figure 4d actually demonstrates that correlation coefficient between T_{exo} and Ap + $F_{10.7}$ is $R = 0.8$ (so that $R^2 = 0.64$) during the period of interest, which is around the recent solar minimum (daily Ap = 0–42; $F_{10.7}$ = 67–113). It is a new finding in this study that T_{exo} can be parameterized better by Ap + $F_{10.7}$ than by only one of the indices. As the coefficient of determination, $R^2 = 0.64$, ~64% of T_{exo} day-to-day variation can be explained by Ap + $F_{10.7}$. The thick black dashed line in Figure 4d is the linear regression to the data points, of which the equation and Mean-Absolute-Error
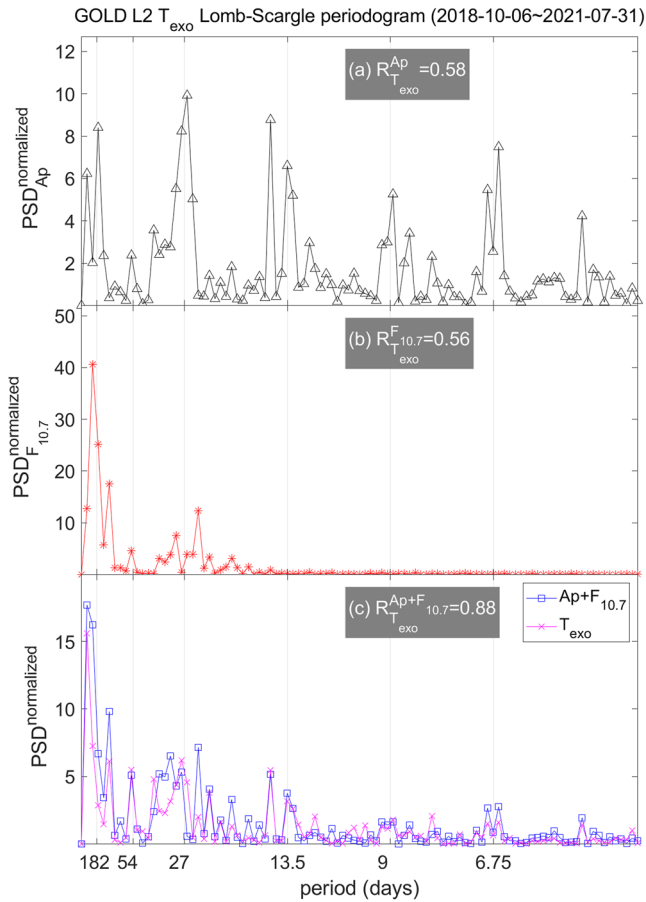
Figure 5. Lomb-Scargle periodograms of (a) Ap, (b) $F_{10.7}$, and (c) Ap + $F_{10.7}$. That of GOLD T_{exo} is overlaid in the bottom panel with magenta color. The Power Spectral Density (PSD) on the vertical axes is normalized by twice the variance. In each panel, the correlation coefficient between the periodogram of the geophysical index and that of T_{exo} is given.

(MAE) are annotated inside the panel (MAE$_{linear}$). The MAE between the linear estimate and actual T_{exo} is only about 9.4 K. The regression equation, $T_{exo} = 2.3 \times (Ap + F_{10.7}) + 646.9$ (K) can be used as a rule of thumb in estimating exospheric temperature with geomagnetic and solar indices. We have tried slightly different weights for the linear combination of Ap and $F_{10.7}$ (Ap + 0.8 × $F_{10.7}$ and Ap + 1.2 × $F_{10.7}$), but the results are qualitatively the same with the correlation coefficient around 0.8. We have also made figures similar to Figure 4d using subsets of GOLD T_{exo} (i.e., only prenoon/postnoon or equatorial/off-equatorial regions: figures not shown). The correlation coefficients do not improve much from the value ($R = 0.8$) in Figure 4d. The thin black dashed lines in Figure 4d mark the 95% prediction interval (~28 K from the regression line). Finally, the red dashed line represents the second-order polynomial fit to the data points. Its MAE (MAE$_{quad}$ = 8.8 K) is similar to that of the linear fit (9.4 K), which means that it does not drastically improve the T_{exo} prediction ability.

In Figure 5, we present the Lomb-Scargle periodograms of (a) Ap, (b) $F_{10.7}$, and (c) Ap + $F_{10.7}$. Lomb-Scargle analysis estimates strength of periodic variations in time series data (e.g., Scargle, 1982). From the results, we can identify embedded periodicity of T_{exo} and geophysical indices such as Ap and $F_{10.7}$. The corresponding periodogram of T_{exo} is overlaid in the bottom panel as magenta symbols. The Power Spectral Density (PSD) on the vertical axes is normalized by two times the variance of the respective variables. In each panel, the correlation coefficient of the periodogram (solar/geomagnetic indices) with that of T_{exo} is annotated. In Figure 5a, the Ap index exhibits conspicuous periodicities at harmonics of solar rotation (e.g., 27, 13.5, 9, and 6.75 days) in addition to those with ≥182 days (e.g., semiannual and annual variations). The harmonics of the 27-day solar rotation are as expected for geomagnetic activity during solar-minimum years (e.g., Lei et al., 2008, Figure 1). On the other hand, $F_{10.7}$ in Figure 5b mainly shows the ≥182-day and 27-day periodicities: the absence of 13.5-day and 9-day harmonics also agrees with Lei et al. (2008, Figure 1). The periodogram of GOLD T_{exo} in Figure 5c (magenta) appears similar to neither Figure 5a (Ap) nor Figure 5b ($F_{10.7}$). This visual impression is confirmed by the correlation coefficients in Figures 5a and 5b that have only moderate magnitudes. However, the periodogram for the combined index of Ap + $F_{10.7}$ (Figure 5c) is highly correlated with that of GOLD T_{exo} with the correlation coefficient as high as 0.88. The overall results in Figure 5 (periodograms) confirm those of Figure 4 (scatterplots) in that Ap + $F_{10.7}$ predicts T_{exo} better than either Ap or $F_{10.7}$ in isolation.

3.3. Correlation of GOLD T_{exo} With Other Thermospheric Data at Various Altitudes

Figure 6 presents scatterplots of GOLD T_{exo} with a variety of thermospheric parameters that represent different altitude ranges: (a) GOLD T_{disk} at ~150 km, (b) GOLD O_2 density at ~170 km, (c) thermospheric mass density measured by the accelerometer onboard Swarm-Charlie (altitude ~ 450 km), (d and e) neutral temperature at ~100 km measured by ICON/MIGHTI-A and Aura/MLS, and (f) TCI estimated from the TIMED/SABER data (representative altitude ~130 km). Note that all the points in Figure 6 represent daily averages. We only use the central part of each GOLD T_{disk} image (±25% of the image side length from the center) to reduce effects of near-edge regions. We omit high-latitude Aura/MLS data beyond ±40° GLAT. The correlation coefficient (R) between the horizontal and vertical axis is annotated in each panel. For Figure 6b (GOLD O_2 density at ~170 km), through linear fitting to the data points, outliers (gray symbols) whose residuals are beyond three standard deviations are omitted in estimating the robust correlation coefficient (R_{robust}). The procedure of outlier removal is iterated until no additional data point is discarded. The various correlation coefficients in Figure 6 seem to suggest that T_{exo} is well correlated with thermospheric density/temperature data from altitudes *above* ~130 km. On the contrary,
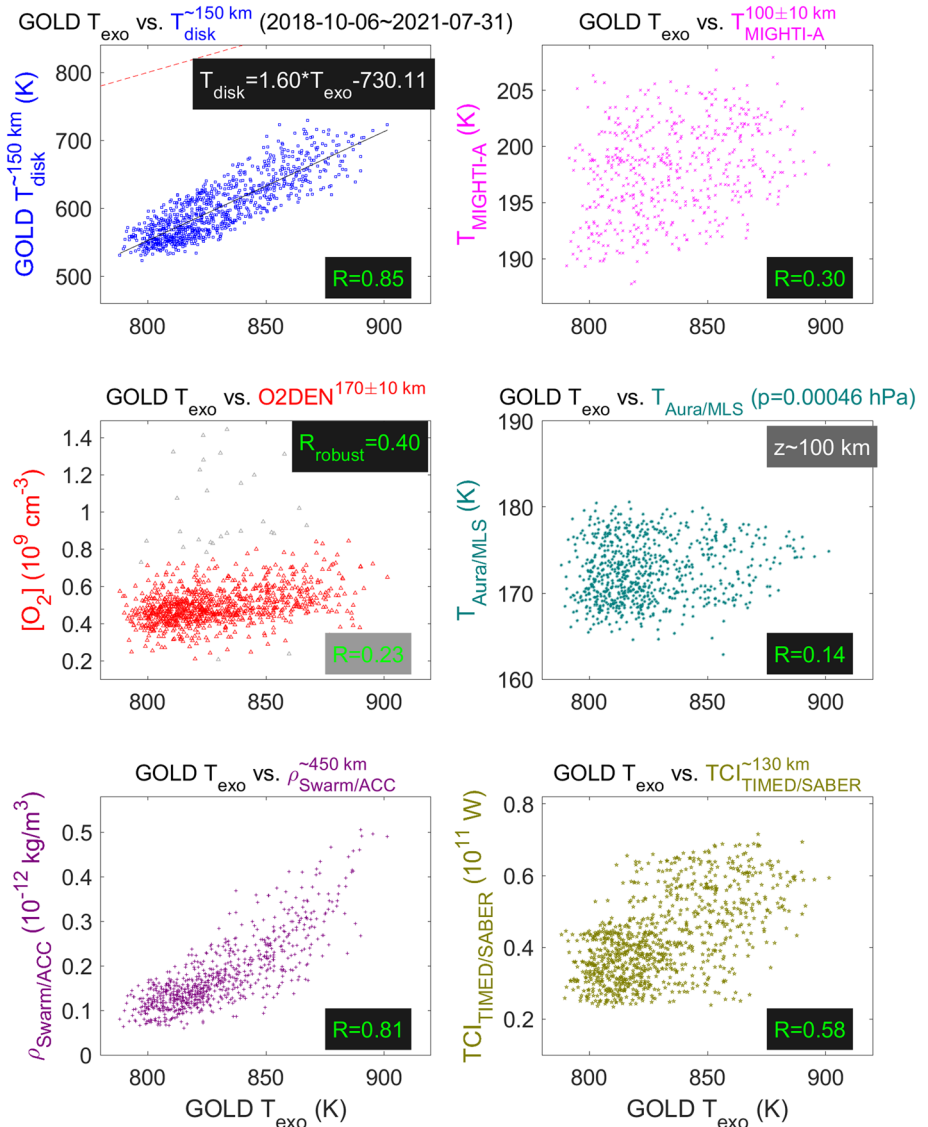
Figure 6. Scatterplots of GOLD T_{exo} with various data sets retrieved from GOLD and other LEO satellites: (a) GOLD T_{disk} relevant to altitudes of ~150 km, (b) GOLD O_2 density relevant to altitudes of ~170 km, (c) thermospheric mass density at altitudes of ~450 km measured by Swarm-Charlie, (d) neutral temperature at altitudes of ~100 km measured by ICON/MIGHTI-A, (e) neutral temperature at pressure level of 0.00046 hPa (~100 km; see Waters et al., 2006, Figure 2) measured by Aura/MLS, and (f) Thermosphere Climate Index (TCI) deduced from the TIMED/SABER measurements around altitudes of 130 km. The red dashed line in panel a represents the line of one-to-one correspondence (i.e., $T_{exo} = T_{disk}$). The black solid line in panel a represents the polynomial fit, whose equation is annotated within the panel.

the correlation becomes very low *below* that altitude (e.g., ~100 km above the surface): see the area highlighted with a purple dashed rectangle.

One may question whether the poor correlation between T_{exo} and temperature at ~100-km altitude (from either Aura/MLS or ICON/MIGHTI) might result from data quality issues, if any, of the latter. We have made a correlation diagram of Aura/MLS versus ICON/MIGHTI that is similar to Figure 6 (figure not shown). The Aura/MLS temperature displays good correlation with that of ICON/MIGHTI ($R \sim 0.68$). The result supports reliability of both data sets; to say the least, reliability of their qualitative day-to-day variations.

While the GOLD O2DEN product gives altitude profiles of O_2 density, 170 km is chosen in Figure 6 following Lumpe et al. (2020, Figures 15 and 16). Lumpe et al. (2020, Figure 9) also showed that the GOLD O2DEN is

most reliable around 170 km. Note that we have already corrected altitude errors due to clock drift, following the method recommended by the mission team (https://gold.cs.ucf.edu/wp-content/tools/gold_time_deltas.pdf).

4. Discussion

4.1. Basic Climatology of T_{exo}: Reproduction of Previous Studies

The GOLD T_{exo} data shown in the preceding section generally confirm conclusions in the existing literature. The morning-afternoon asymmetry in Figure 1 (i.e., morning T_{exo} < afternoon T_{exo}) agrees with Mayr et al. (1973), Buonsanto and Pohlman (1998, Figure 2), Weimer et al. (2016, Figure 6), and Weng et al. (2017, Figure 7). Positive dependence on solar activity in Figure 4 conforms to Kelley et al. (1983), Buonsanto and Pohlman (1998, Figures 7 and 9), Smithtro and Sojka (2005b, Figure 3), Meier et al. (2015, Figure 20), Weng et al. (2017, Figures 2 and 5), Ruan et al. (2018, Figure 1), and Evans et al. (2020, Figure 8). Positive dependence on geomagnetic activity in Figure 4 is consistent with Choury et al. (2013, Figure 1) and Evans et al. (2020, Figures 8 and 9).

Weak seasonal variation of the GOLD T_{exo} was found in Figure 1. The weak seasonality may be attributed to the fact that a summer-winter distinction is not very meaningful near the equator, which is the region relevant to the GOLD T_{exo} data (approximately $\pm 10°$ GLAT). Note also that our data set spans the years 2019–2021, which surround the latest solar minimum. According to Kelley et al. (1983), seasonal variation of T_{exo} is weaker under weaker solar activity, which may explain the inconspicuous seasonal dependence in Figure 1.

In Figures 1a–1c, we find an equatorial peak of T_{exo} around local noon, which is very confined latitudinally (GLAT extent <10°). This feature could not be seen in Weimer et al. (2020, Figure 4), and we would like to be careful in interpreting this equatorial peak. If we separate the western (Pacific; Figures 1a–1c) and eastern (African; Figures 1d–1f) limb data, the equatorial peak of T_{exo} in Figure 1 is much more conspicuous in the former. If this is a true geophysical phenomenon, its absence in Weimer et al. (2020) may be attributed to the coarse resolution (∼7°) and/or different (i.e., relatively high) solar activity (note the use of the CHAMP satellite in that study). Climatology based on longer data sets would be necessary to confirm the veracity of the near-noon equatorial peak in the GOLD western (Pacific; Figures 1a–1c) limb.

The general behavior of GOLD T_{exo} in Figures 1 and 2 is also consistent with studies at Venus and Mars. For example, Niemann et al. (1998, Figure 2) and Stone et al. (2018, Figures 20 and 21) also reported that T_{exo} is higher in the afternoon than in the morning. Positive dependence of T_{exo} on solar activity was reported by Bougher et al. (2009, Figure 1): see also Bougher et al. (2017, Figure 8). Additionally, persistent enhancement at the dusk terminator (Figure 1) was recently reported for Mars (Gupta et al., 2019).

4.2. Comparison With Other Contemporaneous Data

Figure 6 presented correlation diagrams of GOLD T_{exo} with various thermospheric parameters representative of various altitudes. In Figure 6a, the GOLD T_{disk}, which represents thermospheric temperature at ∼150 km (Krier et al., 2021), is well correlated ($R = 0.85$) with GOLD T_{exo}. This is consistent with previous studies: temperature at altitudes around 150 km was reported to be correlated to T_{exo} (e.g., Meier et al., 2015, Figures 15 and 16): see also Zhang et al. (2019, p. 5854). Also, Laskar, Eastes, et al. (2021) demonstrated that GOLD T_{disk} is sensitive to solar and geomagnetic activity, as GOLD T_{exo} is in our study. The red dashed line in Figure 6a represents the line of one-to-one correspondence (i.e., $T_{exo} = T_{disk}$), according to which GOLD T_{exo} is always larger than T_{disk} by about 250 K. This difference between T_{exo} and T_{disk} at 150-km altitude is in qualitative agreement with recent simulations by Laskar, Pedatella, et al. (2021, Figures 6 and 7). The black solid line in Figure 6a represents the polynomial fit between T_{exo} and T_{disk}, of which the equation is annotated within the panel.

Figure 6c shows good correlation ($R = 0.81$) between GOLD T_{exo} and thermospheric mass density measured by Swarm-Charlie accelerometer at ∼450-km altitudes. This is also consistent with previous studies. For example, Weng et al. (2017, Figure 5) showed that overall variations of daily averaged T_{exo} are consistent with those of thermospheric mass density. Note that thermospheric mass density can also be derived from the precise orbit determination (POD) data of Swarm. The product name is DNSxPOD, where x is either A, B, or C representing one specific satellite: the data are available at the official Swarm repository. We have replaced the DNSCACC data in Figure 6c with DNSCPOD, and obtained similar results with a slightly improved correlation coefficient ($R = 0.85$, figures not shown), which supports robustness of our results.

In Figure 6f, we show that the correlation coefficient between GOLD T_{exo} and TIMED/SABER TCI is moderate ($R = 0.58$). According to Mlyczak et al. (2018b), NO emission, which is represented by the TCI, is a sensitive indicator of temperature. Hence, the TCI in Figure 6f can be deemed a proxy for temperature at ~130 km, the peak altitude of NO emission (Mlynczak et al., 2018a, and references therein). The correlation between TCI and T_{exo} is not a new finding, but in agreement with Weimer et al. (2015) and Weimer et al. (2016, Figure 8): see also Mlynczak et al. (2018a, Summary).

Figure 6b illustrates that O_2 density at 170 km is still positively correlated with GOLD T_{exo}, but the correlation coefficient is smaller than in Figure 6a (GOLD T_{disk}; ~150 km) and Figure 6c (Swarm mass density; ~450 km). We note that O_2 is a minor constituent at 120–240-km altitudes (Smithtro & Sojka, 2005a, Figure 2), to which GOLD O2DEN data are relevant (https://gold.cs.ucf.edu/data/documentation/). At those altitudes, the dominant neutrals are N_2 (at lower altitudes) and O (at higher altitudes). According to Russell (2011, Section 4), thermospheric (>120 km) O_2 variations do not strictly follow those of the dominant elements (N_2 and O): e.g., O_2 and O changes are shown to be nearly anticorrelated by Russell (2011, Figure 4.42). Therefore, the O_2 density variations are only moderately correlated with the total neutral density changes (Russell, 2011, Figures 4.31–4.32). Assuming that the total neutral density is correlated with T_{exo}, the results presented by Russell (2011) can explain our Figure 6b, which shows moderate correlation between GOLD O2DEN and GOLD T_{exo}. Furthermore, T_{exo} is not the only driver of the total neutral density (e.g., neutral composition effects), which can further compromise the correlation between GOLD O2DEN and GOLD T_{exo}. As the work by Russell (2011) is based only on numerical simulations, our results give the *first observational support* for the moderate correlation between O_2 density at 170 km and T_{exo}. These results are compatible with Lumpe et al. (2020, Figure 15), where GOLD O2DEN exhibits limited correlation with Ap or $F_{10.7}$, both of which (as shown in our Figure 4) are strongly correlated with T_{exo}. Similarly, Aikin et al. (1993, Figure 6) showed relatively poor correlation between O_2 density and $F_{10.7}$. Note that the next version of the GOLD O2DEN product will include a complete correction for the clock drift problem, which will allow us to draw more quantitative conclusions on the correlation between GOLD O_2 and T_{exo} data. Outliers in Figure 6b may be resolved in the next version of the GOLD O2DEN.

In fact, photochemistry, diffusion, and dynamics can all be important for O_2 variability (e.g., Kayser, 1980). The O_2 reacts with a variety of atmospheric/ionized constituents, such as nitrogen, oxygen, and hydrogen neutrals/ions (see, e.g., Russel, 2011, Tables 2.1–2.4). They can also undergo photolysis by solar Lyman-alpha and the Schumann-Runge continuum (Christensen et al., 2012). At altitudes of ~140–200 km, recombination with nitrogen atoms can drive O_2 chemical loss (Siskind et al., 2006). Some of the rate coefficients have large uncertainty, such as O_2 and O rate coefficient mentioned in Mlynczak et al. (2013), which suggests that further studies are warranted for thermospheric O_2.

In Figures 6d and 6e, GOLD T_{exo} exhibits poor correlation with neutral temperature observed below 110 km. Below we discuss three heating agents for the thermosphere *above* 110 km, which can also be related to T_{exo}: Joule heating, particle precipitation, and insolation. We note that Joule heating per scale height is highest around 125 km (Huang et al., 2012, Figure 1), and concomitant neutral temperature changes hardly penetrate down to ~110 km (Huang et al., 2012, Figure 2): see also Lu et al. (2016, Figure 7). The Joule heating heavily depends on geomagnetic activity (Lu et al., 2010, Figure 5), which is in turn correlated with T_{exo}. Nesse Tyssøy et al. (2010) reported similar results that particle precipitation heating rarely penetrates below 100 km. Similarly, neutral temperatures below 150 km are not immediately affected by changes in Extreme Ultraviolet (EUV) insolation: see Yan et al. (2021, Figure 5). According to Woods et al. (2000, Figure 2), Far-Ultraviolet (FUV) solar radiation in the wavelength range of 120–180 nm (e.g., the Schumann-Runge continuum) is largely absorbed near and above 100 km. Also, the heating rate of O_2 and O_3 by solar ultraviolet radiation is lower around 100-km altitudes than above (Feofilov & Kutepov, 2012, Figure 15). Thus, we expect poor correlation between the GOLD T_{exo}, which is well correlated with $F_{10.7}$ (solar activity), and the ICON/MIGHTI and Aura/MLS temperatures (~100 km). IR radiative cooling in the lower thermosphere around 100 km (e.g., Dickinson, 1984) can further decrease the correlation between T_{exo} and temperature around ~100 km. Our Figures 6d and 6e confirm this expectation.

The limited agreement between the temperature at altitudes of ~100 km (MIGHTI and MLS temperature) and T_{exo} is also compatible with a number of previous studies on the lower thermosphere. Lee et al. (2013) and Yi et al. (2017) reported *absence* of 7-day, 9-day, and 13-day oscillations in the Aura/MLS temperature data. As those oscillations are generally attributed to recurrent geomagnetic activity, the results in Lee et al. (2013) and Yi et al. (2017) suggest that the Aura/MLS temperatures are not well correlated with geomagnetic activity, unlike

T_exo. Also, the limited correlation can be interpreted in the context of Smithtro and Sojka (2005b) and Forbes et al. (2011). Smithtro and Sojka (2005b, Section 6.1) reported simulation results showing that T_exo is insensitive to the conditions around 95 km. In Forbes et al. (2011), tidal variations of T_exo are found to be dominated by those generated above 110 km, which would contribute to different behavior of the temperature below 110 km and T_exo. Still, the previous studies only provide circumstantial evidence for the poor correlation between the temperature below 110 km and T_exo, whereas our study gives direct observational evidence.

Finally, we note a recent study by Huang and Vanyo (2021) for atmospheric temperature below 100-km altitude (89–97 km) at low latitudes. In their Figure 6, *annual* averages of the atmospheric temperature (i.e., one value per year) display positive correlation with $F_{10.7}$ and Ap. Hence, it would be warranted to compare *annual* averages of T_exo and temperature below 110 km: we can see if their correlation will get better than in our results, which are based on *daily* averages. In the current study, only two data points (for years 2019 and 2020) are available for complete *annual* averages of GOLD TLIMB (T_exo), which are insufficient for correlation analyses. This topic is reserved for future works when more GOLD TLIMB data (at least for one solar cycle) become available.

4.3. Comparison With MSIS2.0

In this section, we investigate whether the behavior of the observation data in Section 3 is reproduced by the empirical MSIS model. To this aim, we run the MSIS2.0 model (https://pypi.org/project/pymsis/) with the input of the GLAT, GLON, time of every GOLD T_exo data point. We use MSIS neutral temperature at 5,000 km for comparison with GOLD T_exo. For the same (GLAT, GLON, time), we also run the MSIS2.0 for neutral temperature at 150 km (corresponding to Figure 6a of GOLD T_disk) and 100 km (corresponding to Figure 6d of ICON/MIGHTI temperature) as well as molecular oxygen at 170-km altitude (corresponding to Figure 6b of GOLD-O2DEN) and total mass density at 450 km (corresponding to Figure 6c of Swarm mass density data). Hourly Ap at the GOLD observations and $F_{10.7}$ as well as its 81-day averages are input to MSIS2.0.

Figure 7 is the same as Figure 1, but with MSIS2.0 results. The following differences from Figure 1 are noteworthy. First, the overall T_exo is lower for MSIS than GOLD. For example, the mean of the equatorial (|GLAT| < 5°) bins in Figure 1a is 846 K while it is only 793 K in Figure 7a. In the western limb (Figures 7a–7c), note that MSIS-T_exo at 15:00–16:00 is larger than in earlier SLTs. This possibly results from poor bin population at 15:00–16:00. The GOLD western limb observations (Figures 1a–1c) have only a few data points per bin for the 15:00–16:00 SLT, and the MSIS result in Figure 7 is obtained per GOLD observation. Second, near-dusk high T_exo in Figures 1d–1f is absent in Figure 7. On the one hand, this discrepancy supports the caveat for the magnitude of near-dusk GOLD T_exo discussed in Section 3. On the other hand, it may suggest a possibility that MSIS2.0 be lacking the physics of dusk terminator enhancement reported by Gupta et al. (2019). Further studies are warranted to investigate the duskside hotspot in GOLD T_exo. Third, the near-noon equatorial peak that is visible in the GOLD western limb data (Figures 1a–1c) is not present in MSIS (Figures 7a–7c).

Figure 8 is the same as Figure 4, but with MSIS2.0 results. The most conspicuous difference from Figure 4 is the fact that T_exo correlates well with $F_{10.7}$ ($R = 0.73$), but not with Ap ($R = 0.18$). The combination of the two (Figure 8d) exhibits poorer correlation with T_exo than $F_{10.7}$ alone (Figure 8b). In summary, the effect of Ap on GOLD T_exo is under-represented in MSIS2.0.

Figure 9 is the same as Figure 6, but with MSIS2.0 results. Panels e and f are omitted in Figure 9 because Figure 6e represents similar altitudes to those of Figure 6d, and Figure 6f presents the TCI index that cannot be directly provided by MSIS2.0. The positive correlation of MSIS-T_exo with temperature at 150 km (Figure 9a) and with total density at 450 km (Figure 9c) agrees with Figures 6a and 6c. The poor correlation between MSIS-T_exo and temperature at 100 km (Figure 9d) also agrees with Figure 6d. However, MSIS O_2 density at 170 km (Figure 9b) is anticorrelated with MSIS-T_exo ($R = -0.5$), contrary to the observation results in Figure 6b.

To summarize, (a) MSIS-T_exo is generally smaller in magnitude than GOLD T_exo, (b) MSIS-T_exo exhibits weaker dependence on Ap than GOLD T_exo, and (c) the T_exo-O2DEN relationship is reversed between MSIS2.0 and GOLD. With the limited amount of data used in this study, we cannot draw a decisive conclusion as to whether MSIS2.0 or GOLD better represents the actual conditions. Further studies are warranted to resolve this discrepancy.
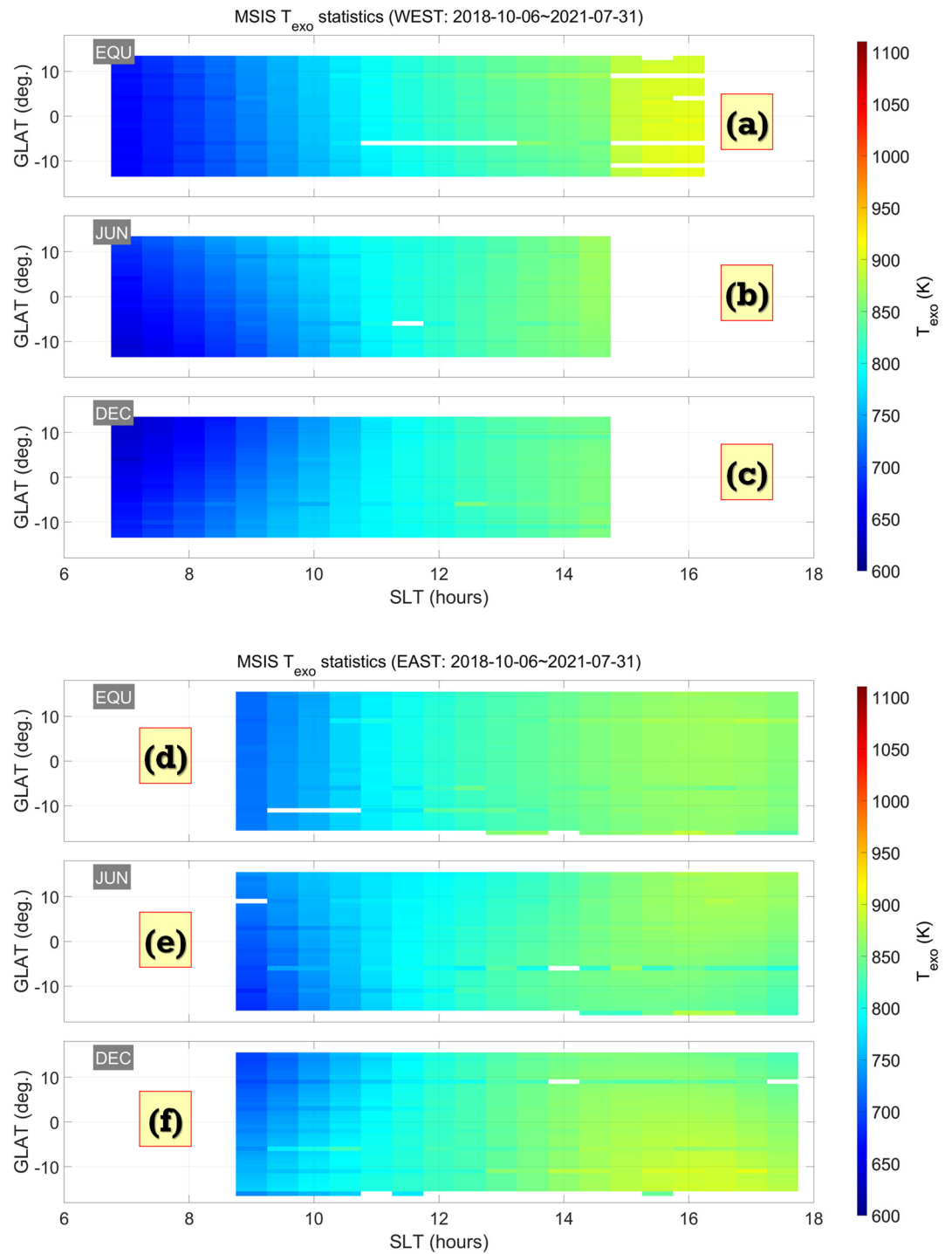
Figure 7. Similar to Figure 1, but presenting MSIS2.0 T_{exo} instead of GOLD T_{exo}.

5. Summary and Conclusion

Using the GOLD Level-2 TLIMB data product, we have conducted an extensive investigation on the low-latitude dayside exospheric temperature in years 2018–2021, during which the daily Ap and $F_{10.7}$ indices were 0–42 (median = 4) and 63–113 (median = 70), respectively. This study is a follow-up of the first analysis of GOLD T_{exo} by Evans et al. (2020). Our statistical results confirm previous studies on the terrestrial, Martian, and Venusian
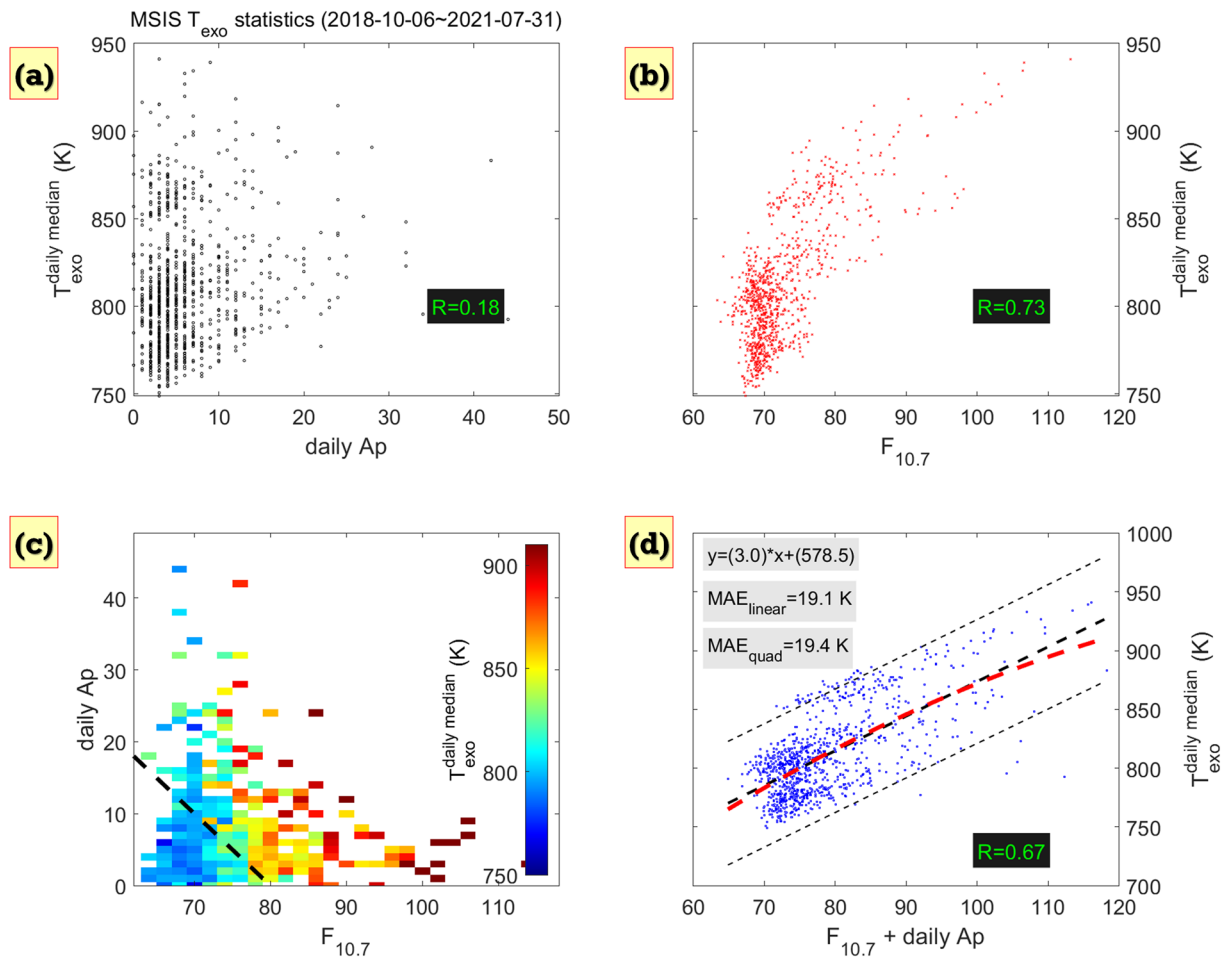
Figure 8. Similar to Figure 4, but presenting MSIS2.0 T_{exo} instead of GOLD T_{exo}.

exosphere, such as morning-afternoon asymmetry and positive dependence on Ap and $F_{10.7}$. Additionally, there are new findings in this study, which can be summarized as follows:

1. Though T_{exo} has been known to be correlated with either Ap or $F_{10.7}$, their arithmetic sum is better aligned with the T_{exo} distribution and can explain $\sim 64\%$ (R^2) of its day-to-day variability
2. Daily averaged T_{exo} exhibits positive correlation with thermospheric parameters representative of altitudes above ~ 110 km: neutral mass density (450 km), neutral temperature (150 km), and NO emission (130 km). On the contrary, the daily average T_{exo} is poorly correlated with ICON/MIGHTI and Aura/MLS temperatures, both of which represent altitudes around 100 km. As MSIS2.0 reproduces this feature, it can be considered as *implicitly* known to the community
3. Daily averaged T_{exo} is moderately correlated with O_2 density at 170 km, where it is a nonnegligible but minor species. This first observational result supports previous numerical simulations by Russell (2011)
4. In comparison with GOLD T_{exo}, MSIS-T_{exo} is generally smaller in magnitude and has weaker correlation with Ap. The T_{exo}-O2DEN relationship is reversed between MSIS2.0 (negative correlation) and GOLD (positive correlation). Duskside T_{exo} hotspots in GOLD data do not appear in MSIS2.0, which warrants further investigation

Overall, T_{exo} at dayside low latitudes is: (a) controlled by solar and geomagnetic activity and; (b) affects many thermospheric parameters down to ~ 130 km, below which drivers of T_{exo} variability appear to have weaker effects than above. The poor correlation between T_{exo} and neutral temperature around 100 km demonstrates that one source of information cannot be substituted with the other. Hence, we need both data sets for accurate specification of the whole atmosphere, e.g., as boundary conditions for global circulation models.
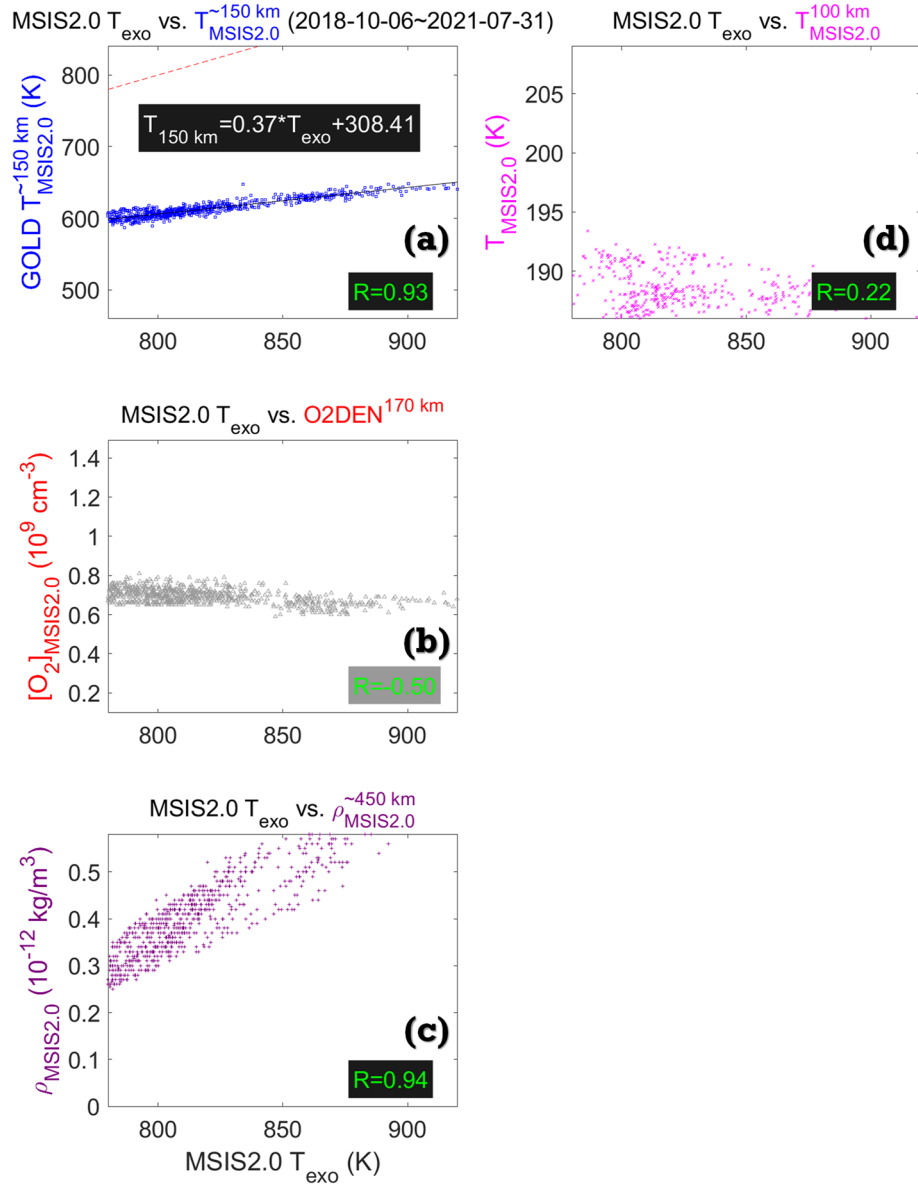
Figure 9. Similar to Figure 6, but presenting MSIS2.0 instead of actual satellite data.

Finally, we list a few limitations of the GOLD T_{exo} data. First, we cannot deduce a global climatology of T_{exo} as shown in Weimer et al. (2020). GOLD can observe T_{exo} at only two GLON sectors (Eastes et al., 2020, Figure 5), and only daytime data are available, which hinders us from investigating GLON dependence on a global scale and from conducting extensive tidal analyses as in Forbes et al. (2011). Second, GOLD experienced only low and moderate solar activity until recently (e.g., Lumpe et al., 2020). Thus, analyzing a larger set of GOLD data spanning the forthcoming solar maximum would be beneficial to understanding the behavior of T_{exo} more thoroughly.

Data Availability Statement

The GOLD data and quicklook images are available at: https://gold.cs.ucf.edu/data/search/. The official repository of the Swarm mission is https://swarm-diss.eo.esa.int/#swarm. The ICON data are open to the public at: https://icon.ssl.berkeley.edu/Data. Aura/MLS Level-3 data can be downloaded from https://acdisc.gesdisc.eosdis.nasa.gov/data/Aura_MLS_Level3/ML3DZT.005/. TIMED/SABER TCI are open to public at https://www.space-weather.com/images2021/08sep21/tci_info.txt.

References

Aikin, A. C., Hedin, A. E., Kendig, D. J., & Drake, S. (1993). Thermospheric molecular oxygen measurements using the ultraviolet spectrometer on the Solar Maximum Mission spacecraft. *Journal of Geophysical Research*, *98*(A10), 17607–17613. https://doi.org/10.1029/93JA01468

Bougher, S. W., McDunn, T. M., Zoldak, K. A., & Forbes, J. M. (2009). Solar cycle variability of Mars dayside exospheric temperatures: Model evaluation of underlying thermal balances. *Geophysical Research Letters*, *36*, L05201. https://doi.org/10.1029/2008GL036376

Bougher, S. W., Roeten, K. J., Olsen, K., Mahaffy, P. R., Benna, M., Elrod, M., et al. (2017). The structure and variability of Mars dayside thermosphere from MAVEN NGIMS and IUVS measurements: Seasonal and solar activity trends in scale heights and temperatures. *Journal of Geophysical Research: Space Physics*, *122*, 1296–1313. https://doi.org/10.1002/2016JA023454

Buonsanto, M. J., & Pohlman, L. M. (1998). Climatology of neutral exospheric temperature above Millstone Hill. *Journal of Geophysical Research*, *103*(A10), 23381–23392. https://doi.org/10.1029/98JA01919

Choury, A., Bruinsma, S., & Schaeffer, P. (2013). Neural networks to predict exosphere temperature corrections. *Space Weather*, *11*, 592–602. https://doi.org/10.1002/2013SW000969

Christensen, A. B., Yee, J.-H., Bishop, R. L., Budzien, S. A., Hecht, J. H., Sivjee, G., & Stephan, A. W. (2012). Observations of molecular oxygen Atmospheric band emission in the thermosphere using the near infrared spectrometer on the ISS/RAIDS experiment. *Journal of Geophysical Research*, *117*, A04315. https://doi.org/10.1029/2011JA016838

Dickinson, R. E. (1984). Infrared radiative cooling in the mesosphere and lower thermosphere. *Journal of Atmospheric and Terrestrial Physics*, *46*(11), 995–1008. https://doi.org/10.1016/0021-9169(84)90006-0

Eastes, R. W., McClintock, W. E., Burns, A. G., Anderson, D. N., Andersson, L., Aryal, S., et al. (2020). Initial observations by the GOLD mission. *Journal of Geophysical Research: Space Physics*, *125*, e2020JA027823. https://doi.org/10.1029/2020JA027823

Emmert, J. T., Drob, D. P., Picone, J. M., Siskind, D. E., Jones, M., Mlynczak, M. G., et al. (2021). NRLMSIS 2.0: A whole-atmosphere empirical model of temperature and neutral species densities. *Earth and Space Science*, *8*, e2020EA001321. https://doi.org/10.1029/2020EA001321

Englert, C. R., Harlander, J. M., Brown, C. M., Marr, K. D., Miller, I. J., Eloise Stump, J., et al. (2017). Michelson interferometer for global high-resolution thermospheric imaging (MIGHTI): Instrument design and calibration. *Space Science Reviews*, *212*, 553–584. https://doi.org/10.1007/s11214-017-0358-4

Evans, J. S., Lumpe, J. D., Correira, J., Veibell, V., Kyrwonos, A., McClintock, W. E., et al. (2020). Neutral exospheric temperatures from the GOLD mission. *Journal of Geophysical Research: Space Physics*, *125*, e2020JA027814. https://doi.org/10.1029/2020JA027814

Feofilov, A., & Kutepov, A. (2012). Infrared radiation in the mesosphere and lower thermosphere: Energetic effects and remote sensing. *Surveys in Geophysics*, *33*, 1231–1280. https://doi.org/10.1007/s10712-012-9204-0

Forbes, J. M., Lemoine, F. G., Bruinsma, S. L., Smith, M. D., & Zhang, X. (2008). Solar flux variability of Mars' exosphere densities and temperatures. *Geophysical Research Letters*, *35*, L01201. https://doi.org/10.1029/2007GL031904

Forbes, J. M., Zhang, X., Bruinsma, S., & Oberheide, J. (2011). Sun-synchronous thermal tides in exosphere temperature from CHAMP and GRACE accelerometer measurements. *Journal of Geophysical Research*, *116*, A11309. https://doi.org/10.1029/2011JA016855

Gupta, N., Venkateswara Rao, N., & Kadhane, U. R. (2019). Dawn-dusk asymmetries in the Martian upper atmosphere. *Journal of Geophysical Research: Planets*, *124*, 3219–3230. https://doi.org/10.1029/2019JE006151

Huang, T.-Y., & Vanyo, M. (2021). Trends in the airglow temperatures in the MLT region—Part 2: SABER observations and comparisons to model simulations. *Atmosphere*, *12*, 167. https://doi.org/10.3390/atmos12020167

Huang, Y., Richmond, A. D., Deng, Y., & Roble, R. (2012). Height distribution of Joule heating and its influence on the thermosphere. *Journal of Geophysical Research*, *117*, A08334. https://doi.org/10.1029/2012JA017885

Immel, T. J., England, S. L., Mende, S. B., Heelis, R. A., Englert, C. R., Edelstein, J., et al. (2018). The ionospheric connection explorer mission: Mission goals and design. *Space Science Reviews*, *214*, 13. https://doi.org/10.1007/s11214-017-0449-2

Kayser, D. (1980). Solar flux variation of the thermospheric molecular oxygen density. *Journal of Geophysical Research*, *85*(A2), 695–702. https://doi.org/10.1029/JA085iA02p00695

Kelly, J. D., Heinselman, C. J., & Petriceks, J. (1983). High-latitude exospheric temperature observed over a solar cycle. *Radio Science*, *18*(6), 901–905. https://doi.org/10.1029/RS018i006p00901

Kil, H., Lee, W. K., & Paxton, L. J. (2020). Origin and distribution of daytime electron density irregularities in the low-latitude F region. *Journal of Geophysical Research: Space Physics*, *125*, e2020JA028343. https://doi.org/10.1029/2020JA028343

Krier, C. S., England, S. L., Greer, K. R., Scott Evans, J., Burns, A. G., & Eastes, R. W. (2021). Deducing non-migrating diurnal tides in the middle thermosphere with GOLD observations of the Earth's far ultraviolet dayglow from geostationary orbit. *Journal of Geophysical Research: Space Physics*, *126*, e2021JA029563. https://doi.org/10.1029/2021JA029563

Laskar, F. I., Eastes, R. W., Codrescu, M. V., Evans, J. S., Burns, A. G., Wang, W., et al. (2021). Response of GOLD retrieved thermospheric temperatures to geomagnetic activities of varying magnitudes. *Geophysical Research Letters*, *48*, e2021GL093905. https://doi.org/10.1029/2021GL093905

Laskar, F. I., Pedatella, N. M., Codrescu, M. V., Eastes, R. W., Evans, J. S., Burns, A. G., & McClintock, W. (2021). Impact of GOLD retrieved thermospheric temperatures on a whole atmosphere data assimilation model. *Journal of Geophysical Research: Space Physics*, *126*, e2020JA028646. https://doi.org/10.1029/2020JA028646

Lee, Y.-S., Kirkwood, S., Shepherd, G. G., Kwak, Y.-S., & Kim, K.-C. (2013). Long-periodic strong radar echoes in the summer polar D region correlated with oscillations of high-speed solar wind streams. *Geophysical Research Letters*, *40*, 4160–4164. https://doi.org/10.1002/grl.50821

Lei, J., Thayer, J. P., Forbes, J. M., Sutton, E. K., Nerem, R. S., Temmer, M., & Veronig, A. M. (2008). Global thermospheric density variations caused by high-speed solar wind streams during the declining phase of solar cycle 23. *Journal of Geophysical Research*, *113*, A11303. https://doi.org/10.1029/2008JA013433

Li, Q., Hao, Y., Zhang, D., & Xiao, Z. (2018). Nighttime enhancements in the midlatitude ionosphere and their relation to the plasmasphere. *Journal of Geophysical Research: Space Physics*, *123*, 7686–7696. https://doi.org/10.1029/2018JA025422

Lichtenegger, H. I. M., Lammer, H., Kulikov, Y. N., Kazeminejad, S., Molina-Cuberos, G. H., Rodrigo, R., et al. (2006). Effects of low energetic neutral atoms on Martian and Venusian dayside exospheric temperature estimations. *Space Science Reviews*, *126*, 469–501. https://doi.org/10.1007/s11214-006-9082-1

Liu, H., Yamamoto, M., & Lühr, H. (2009). Wave-4 pattern of the equatorial mass density anomaly: A thermospheric signature of tropical deep convection. *Geophysical Research Letters*, *36*, L18104. https://doi.org/10.1029/2009GL039865

Lu, G., Mlynczak, M. G., Hunt, L. A., Woods, T. N., & Roble, R. G. (2010). On the relationship of Joule heating and nitric oxide radiative cooling in the thermosphere. *Journal of Geophysical Research*, *115*, A05306. https://doi.org/10.1029/2009JA014662

Lu, G., Richmond, A. D., Lühr, H., & Paxton, L. (2016). High-latitude energy input and its impact on the thermosphere. *Journal of Geophysical Research: Space Physics*, *121*, 7108–7124. https://doi.org/10.1002/2015JA022294

Lühr, H., Kervalishvili, G. N., Stolle, C., Rauberg, J., & Michaelis, I. (2019). Average characteristics of low-latitude interhemispheric and F region dynamo currents deduced from the swarm satellite constellation. *Journal of Geophysical Research: Space Physics*, *124*, 10631–10644. https://doi.org/10.1029/2019JA027419

Lumpe, J. D., McClintock, W. E., Evans, J. S., Correira, J., Veibell, V., Beland, S., & Eastes, R. (2020). A new data set of thermospheric molecular oxygen from the Global-scale Observations of the Limb and Disk (GOLD) mission. *Journal of Geophysical Research: Space Physics*, *125*, e2020JA027812. https://doi.org/10.1029/2020JA027812

Mayr, H. G., Hedin, A. E., Reber, C. A., & Carignan, G. R. (1973). *Global characteristics in the diurnal variations of the thermospheric temperature and composition*. NASA-TM-66295. Retrieved from https://ntrs.nasa.gov/api/citations/19730018608/downloads/19730018608.pdf

Meier, R., Crowley, G., Strickland, D. J., Christensen, A. B., Paxton, L. J., Morrison, D., & Hackert, C. L. (2005). First look at the 20 November 2003 superstorm with TIMED/GUVI: Comparisons with a thermospheric global circulation model. *Journal of Geophysical Research*, *110*, A09S41. https://doi.org/10.1029/2004JA010990

Meier, R. R., Picone, J. M., Drob, D., Bishop, J., Emmert, J. T., Lean, J. L., et al. (2015). Remote sensing of Earth's limb by TIMED/GUVI: Retrieval of thermospheric composition and temperature. *Earth and Space Science*, *2*, 1–37. https://doi.org/10.1002/2014EA000035

Mikhailov, A. V., & Perrone, L. (2016). Geomagnetic control of the midlatitude daytime foF1 and foF2 long-term variations: Physical interpretation using European observations. *Journal of Geophysical Research: Space Physics*, *121*, 7193–7203. https://doi.org/10.1002/2016JA022716

Mlynczak, M. G., Hunt, L. A., Mast, J. C., Thomas Marshall, B., Russell, J. M., III, Smith, A. K., et al. (2013). Atomic oxygen in the mesosphere and lower thermosphere derived from SABER: Algorithm theoretical basis and measurement uncertainty. *Journal of Geophysical Research: Atmospheres*, *118*, 5724–5735. https://doi.org/10.1002/jgrd.50401

Mlynczak, M. G., Hunt, L. A., & Russell, J. M., Marshall, M. B. T. (2018a). Thermosphere climate indexes: Percentile ranges and adjectival descriptors. *Journal of Atmospheric and Solar-Terrestrial Physics*, *174*, 28–31. https://doi.org/10.1016/j.jastp.2018.04.004

Mlynczak, M. G., Knipp, D. J., Hunt, L. A., Gaebler, J., Matsuo, T., Kilcommons, L. M., & Young, C. L. (2018b). Space-based sentinels for measurement of infrared cooling in the thermosphere for space weather nowcasting and forecasting. *Space Weather*, *16*, 363–375. https://doi.org/10.1002/2017SW001757

Nesse Tyssøy, H., Stadsnes, J., Sørbø, M., Mertens, C. J., & Evans, D. S. (2010). Changes in upper mesospheric and lower thermospheric temperatures caused by energetic particle precipitation. *Journal of Geophysical Research*, *115*, A10323. https://doi.org/10.1029/2010JA015427

Niemann, H. B., Harpold, D. N., Feng, S., Kasprzak, W. T., Way, S. H., Atreya, S. K., et al. (1998). The Planet-B neutral gas mass spectrometer. *Earth, Planets and Space*, *50*, 785–792. https://doi.org/10.1186/BF03352170

Picone, J. M., Hedin, A. E., Drob, D. P., & Aikin, A. C. (2002). NRLMSISE-00 empirical model of the atmosphere: Statistical comparisons and scientific issues. *Journal of Geophysical Research*, *107*(A12), 1468. https://doi.org/10.1029/2002JA009430

Ruan, H., Lei, J., Dou, X., Liu, S., & Aa, E. (2018). An exospheric temperature model based on CHAMP observations and TIEGCM simulations. *Space Weather*, *16*, 147–156. https://doi.org/10.1002/2017SW001759

Russell, A. T. (2011). *Numerical simulations of composition changes in the high latitude thermosphere during disturbed conditions*. The University of Western Ontario. Retrieved from https://ir.lib.uwo.ca/etd/164

Scargle, J. D. (1982). Studies in astronomical time series analysis. II. Statistical aspects of spectral analysis of unevenly spaced data. *The Astrophysical Journal*, *263*, 835–853. https://doi.org/10.1086/160554

Schwartz, M. J., Lambert, A., Manney, G. L., Read, W. G., Livesey, N. J., Froidevaux, L., et al. (2008). Validation of the aura Microwave Limb Sounder temperature and geopotential height measurements. *Journal of Geophysical Research*, *113*, D15S11. https://doi.org/10.1029/2007JD008783

Shepherd, M. G., Meek, C. E., Hocking, W. K., Hall, C. M., Partamies, N., Sigernes, F., et al. (2020). Multi-instrument study of the mesosphere-lower thermosphere dynamics at 80°N during the major SSW in January 2019. *Journal of Atmospheric and Solar-Terrestrial Physics*, *210*, 105427. https://doi.org/10.1016/j.jastp.2020.105427

Siemes, C., de Teixeira da Encarnação, J., Doornbos, E., van den IJssel, J., Kraus, J., Pereštý, R., et al. (2016). Swarm accelerometer data processing from raw accelerations to thermospheric neutral densities. *Earth, Planets and Space*, *68*, 92. https://doi.org/10.1186/s40623-016-0474-5

Siskind, D., Bishop, J., Picone, J., Qian, L., Solomon, S., & Lumpe, J. (2006). *Towards a self consistent picture of odd nitrogen and molecular oxygen chemistry in the thermosphere*. AGU Spring Meeting Abstracts.

Smithtro, C. G., & Sojka, J. J. (2005b). Behavior of the ionosphere and thermosphere subject to extreme solar cycle conditions. *Journal of Geophysical Research*, *110*, A08306. https://doi.org/10.1029/2004JA010782

Smithtro, C. G., & Sojka, J. J. (2005a). A new global average model of the coupled thermosphere and ionosphere. *Journal of Geophysical Research*, *110*, A08305. https://doi.org/10.1029/2004JA010781

Stevens, M. H., Englert, C. R., Harlander, J. M., England, S. L., Marr, K. D., Brown, C. M., & Immel, T. J. (2018). Retrieval of lower thermospheric temperatures from O_2 A band emission: The MIGHTI experiment on ICON. *Space Science Reviews*, *214*, 4. https://doi.org/10.1007/s11214-017-0434-9

Stock, W. (2017). *Estimation of neutral densities in the thermosphere (FYS-3900 Master thesis in Physics)*. Department of Physics and Technology, Arctic University of Norway. Retrieved from https://munin.uit.no/bitstream/handle/10037/11890/thesis.pdf?sequence=2

Stone, S. W., Yelle, R. V., Benna, M., Elrod, M. K., & Mahaffy, P. R. (2018). Thermal structure of the Martian upper atmosphere from MAVEN NGIMS. *Journal of Geophysical Research: Planets*, *123*, 2842–2867. https://doi.org/10.1029/2018JE005559

Swenson, G. R. (1969). Temperature shape parameter of the thermosphere determined from probe data. *Journal of Geophysical Research*, *74*(16), 4074–4078. https://doi.org/10.1029/JA074i016p04074

Waters, J., Froidevaux, L., Harwood, R., Jarnot, R., Pickett, H., Read, W., et al. (2006). The Earth Observing System Microwave Limb Sounder (EOS MLS) on the aura satellite. *IEEE Transactions on Geoscience and Remote Sensing*, *44*, 1075–1092. https://doi.org/10.1109/TGRS.2006.873771

Weimer, D. R., Mehta, P. M., Tobiska, W. K., Doornbos, E., Mlynczak, M. G., Drob, D. P., & Emmert, J. T. (2020). Improving neutral density predictions using exospheric temperatures calculated on a geodesic, polyhedral grid. *Space Weather*, *18*, e2019SW002355. https://doi.org/10.1029/2019SW002355

Weimer, D. R., Mlynczak, M. G., Hunt, L. A., & Tobiska, W. K. (2015). High correlations between temperature and nitric oxide in the thermosphere. *Journal of Geophysical Research: Space Physics*, *120*, 5998–6009. https://doi.org/10.1002/2015JA021461

Weimer, D. R., Sutton, E. K., Mlynczak, M. G., & Hunt, L. A. (2016). Intercalibration of neutral density measurements for mapping the thermosphere. *Journal of Geophysical Research: Space Physics*, *121*, 5975–5990. https://doi.org/10.1002/2016JA022691

Weng, L., Lei, J., Sutton, E., Dou, X., & Fang, H. (2017). An exospheric temperature model from CHAMP thermospheric density. *Space Weather*, *15*, 343–351. https://doi.org/10.1002/2016SW001577

Woods, T. N., Rottman, G. J., Harder, J. W., George, M. L., William, E. M., Greg, A. K., & Chris, P.C. (2000). Overview of the EOS SORCE mission. *Proc. SPIE, Earth Observing Systems V* (Vol. 4135). https://doi.org/10.1117/12.494229

Yan, M., Dang, T., Lei, J., Wang, W., Zhang, S.-R., & Le, H. (2021). From bow waves to traveling atmospheric disturbances: Thermospheric perturbations along solar eclipse trajectory. *Journal of Geophysical Research: Space Physics*, *126*, e2020JA028523. https://doi.org/10.1029/2020JA028523

Yi, W., Reid, I. M., Xue, X., Younger, J. P., Spargo, A. J., Murphy, D. J., et al. (2017). First observation of mesosphere response to the solar wind high-speed streams. *Journal of Geophysical Research: Space Physics*, *122*, 9080–9088. https://doi.org/10.1002/2017JA024446

Zhang, Y., Paxton, L. J., & Schaefer, R. K. (2019). Deriving thermospheric temperature from observations by the global ultraviolet imager on the thermosphere ionosphere mesosphere energetics and dynamics satellite. *Journal of Geophysical Research: Space Physics*, *124*, 5848–5856. https://doi.org/10.1029/2018JA026379